Philippine Journal of Science
152 (3): 989–998, June 2023
ISSN 0031 - 7683
Date Received: 26 May 2022

Microstructures of Austenitic Stainless Steel 56Fe25Ni16.6Cr0.9Si0.5Mn Solid-Treated with Different Cooling Rates

Mohammad Dani[1], Ferhat Aziz[1]*, Parikin Farihin[1], Arbi Dimyati[1], Sulistioso Giat Sukaryo[1], Joshua Gunawan Lesmana[2], Andon Insani[1], Salim Mustofa[1], Mardiyanto Panitra[1], and Ching An Huang[3]

[1]Nuclear Reactor Technology Research Center, National Research and Innovation Agency (BRIN), Kawasan Puspiptek Serpong, Tangerang Selatan 15314 Indonesia
[2]Department of Physics Energy Engineering, Faculty of Clean Energy and Climate Change, Surya University, Kota Tangerang 15143 Indonesia
[3]Department of Mechanical Engineering, Chang Gung University, Taoyuan, Taiwan

A new synthesized 56Fe25Ni16.6Cr0.9Si0.5Mn austenitic stainless steel (ASS) was produced through casting and then annealing and normalizing at 1100 °C, followed by cooling at different rates. Microstructures of the samples were studied by using X-ray and neutron diffractometers, scanning, and transmission electron microscopes. The stainless steel had a face center cubic structure (X-ray diffraction profile). The microstructure of ASS consists of γ-austenite matrix and high Cr carbide particles in the interior grains and grain boundaries. It seemed that the annealing process affected information of γ-austenite grain size in the ASS, growing larger compared to grain size formed in the normalizing process, similarly by cooling into the air, water, and oil media. The $M_{23}C_7$ islands in the grain boundary formed into a larger size after annealing or normalizing processes, and in addition, the island shape was more elongated. No significant changes were found concerning the particle size and shape of M_7C_6 at the grain boundary of the ASS after annealing or normalizing. Neutron diffraction patterns confirmed the Fm3m space group symmetry of ASS as obtained by the XRD method, therefore establishing ASS as an austenite phase. Results of the uniform deformation method (UDM) analysis applied upon the high-resolution powder neutron diffractometer (HRPD) intensity showed that the deformation strain was 2.3705×10^{-4}. TEM results for ASS showed that the sizes of rectangular precipitates ranged from 63 × 32 nm to 84 × 42 nm with larger-sized irregulars reaching about 190 nm across. All these results showed that an ASS has been successfully synthesized and that it has a promising future to be used as a high-temperature structural material.

Keywords: annealing, austenitic stainless steel, casting, microstructure, normalizing, quenching

INTRODUCTION

Austenite stainless steel (ASS) is widely used as a component in many industries due to its excellent combination of high strength, toughness (including creep strength), and good corrosion resistance. Some properties exist due to the presence of major alloying elements such as Cr, Ni, Mn, and Si, as well as additional trace elements such as C, Mo, N, Ti, Sn, Nb, and Al as listed in the tables of austenitic stainless steels (Michael 2008; Xu 2017). These elements are expected to have a contribution to stabilizing the γ-austenite as the ASS matrix and to increase the strength, corrosion, and creep resistance of the

*Corresponding author: ferhat.aziz@brin.go.id

ASS at the elevated temperature through a solid solution, precipitation, or oxide dispersion and carbide hardenings.

Steelmaking techniques are generally developed through powder metallurgy to obtain high-quality steel, where mechanical alloying processes with high-energy milling are involved (Shashanka and Chaira 2014, 2015b). Later, they developed high-temperature steel by adding Y2O3 oxide to the duplex steel system (Shashanka and Chaira 2016), which was previously done *via* computational material simulation (Gupta *et al.* 2015). The material made through the mechanical alloying process is duplex stainless steel (Fe-18Cr-13Ni) with the addition of 1 %wt content of nano yttria and tungsten (Nayak *et al.* 2016).

According to the World Steel Association, in 2016, Indonesia ranks at 24th position in steel production. These may be an opportunity to develop an ASS, even though some additional elements are somewhat difficult to be found. In recent years, various types of stainless steel have been investigated by the author's research group. Dani *et al.* (2018) employed the induction furnace method to synthesize the austenitic 56Fe25Ni16.6Cr0.9Si0.5Mn superalloy. This alloy contains 56 percent by weight (%wt) of Fe, 25 %wt of Ni, 16.6 %wt of Cr, 0.9 %wt of Si, and 0.5 %wt of Mn. It was found that the alloy has an average yield strength of about 430.56 MPa, which is higher than Incoloy A-286.

In parallel, another type of ferritic alloy with a substantial local content has also been produced, labeled as the F1 type of alloy steel (Effendi *et al.* 2012) – namely, 73Fe24Cr2Si0.8Mn0.1Ni (Parikin *et al.* 2018). The main idea behind the synthesis of this composition of ferritic steel was to obtain a new type of ferritic steel materials having both a higher chromium content and a reduced nickel content, hence considerably improving the corrosion resistance properties of the alloy, as reported by Chanda *et al.* (2019). Ferritic steel has usually 10.5–30 %wt chromium content. According to the Schaeffler diagram, a ferritic structure is still formed if the alloy system contains 30 %wt Cr-eq and a maximum of about 6 %wt Ni-eq.

The main goal of this study was to gain much valuable information concerning the quality of the alloy steel material under examination. The main investigations were focused on the crystal and microstructure properties of the alloy obtained by high-resolution powder neutron diffractometer (HRPD) and transmission electron microscope (TEM) technique. This type of steel has been considered a promising candidate for structural material application in nuclear reactors (David *et al.* 2013).

Therefore, as a preliminary study and an ongoing continuation of previous studies on stainless steel, this work will concentrate on the development of 56Fe25Ni16.6Cr0.9Si0.5Mn ASS, which is focused on the study of microstructures – including grain boundary structure after annealing and normalizing with different cooling rates. The steel was treated by a quench-annealed process by heating at a holding temperature of 1100 °C for 30 min and followed by cooling in air, water, and oil. This time-temperature treatment was aimed to refresh the sample, releasing the stress in materials. Various characterization techniques were used to get detailed information on the crystal and fine structure. To obtain information on the mechanical properties in detail, the non-destructive neutron diffraction technique (Withers and Bhadeshia 2001) has been used in the study of strain in materials. For bulk materials and engineering components, neutron diffraction is a technique that is well-established to solve the problem of the non-destructive determination of strain in a material. This is because of the high penetration power of neutrons into the material so that samples with a thickness of several centimeters can be directly measured. In this case, the authors would utilize the uniform deformation method (UDM) to obtain the crystallite diameter size (Å) and the average maximum microstrain (ε).

EXPERIMENTAL METHOD

Smelting of the 56Fe25Ni16.6Cr0.9Si0.5Mn ASS was carried out by casting some steel scraps containing 25 %wt Ni and 16.6 %wt Cr in an induction furnace at more than 1250 °C. The samples were then subjected to annealing and normalizing at 1100 °C for 30 min with different cooling media – namely, in air, water, and fresh oil (SAE 20W-50), respectively. This media was used in this experiment because it was easy to obtain and was widely used by other researchers (Kadhim 2016). Such heating known as solid solution treatment is to dissolve precipitated carbides in the ASS, which was conducted by previous studies (Bhadeshia and Honeycombe 2006; Kazimierz 2015). The element contents in the ASS as-cast were measured by an optical emission spectrometer (OES). The chemical compositions of the ASS and A286 steel as a comparison are listed in Table 1.

To reveal the microstructures of the ASS, the standard metallographic preparations were conducted such as cutting, grinding with emery papers from 220–1500 grit, polishing with 1-µm-sized alumina paste, and etching in a Kaling reagent solution for 10 s.

The steel has a corrosion resistance of approx. 0.06 mpy; sufficient etching time is required to clarify the surface microstructure of the sample. The microstructural observations of the samples were performed using an optical microscope and a Jeol 2506LV scanning electron microscope (SEM) equipped with energy-dispersed X-ray spectrometers. The crystal structure of the ASS was

Table 1. Chemical composition of 56Fe25Ni16.6Cr0.9Si0.5Mn and A286 ASS (%wt).

Element	56Fe25Ni16.6Cr0.9Si0.5Mn ASS	A286 ASS (Latrobe 2009)
C	0.293	0.080
Mn	0.504	0.350
Si	0.890	0.300
Ni	25.040	24.000–27.000
Cr	16.550	13.500–16.000
Mo	–	1.000–1.500
V	–	0.100–0.500
Ti	0.004	1.900
Al	0.003	0.350
B	–	0.010-0.003
P	0.013	–
Fe	Balance	Balance

investigated using a PANalytical X-ray diffractometer (XRD). The neutron diffraction pattern was obtained by using the HRPD neutron diffraction method mounted on the Siwabessy Multi-Purpose Reactor at BRIN. Microstructures of prepared samples were studied with a, H9500 Hitachi TEM operated at a voltage of 300 kV. Thin foil was prepared by using Hitachi FB2200 focused ion beam technique (Dani *et al.* 2015).

RESULTS

XRD Measurements

The XRD results for 56Fe25Ni16.6Cr0.9Si0.5Mn ASS as-cast after solid solution heating and cooling with different rates are shown in Figure 1. All recorded patterns show peaks that are characteristic of Fm3m cubic space symmetry, indicating the austenitic nature of the steel

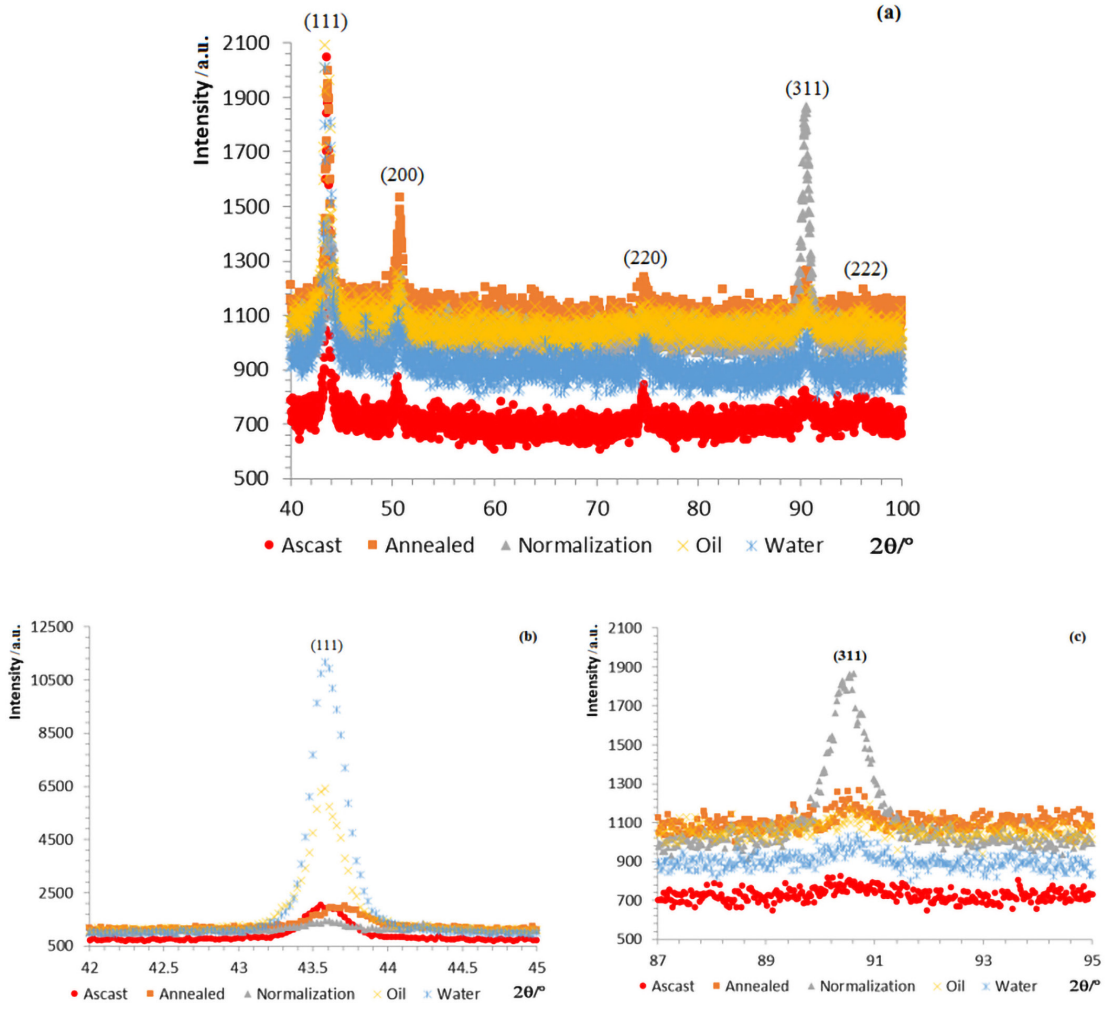

Figure 1. XRD results of [a] all position, [b] (111) plane peak, and [c] (311) plane peak; [red] As-cast, [brown] annealed, [grey] normalized, cooled in air, [blue] normalized, quenched in water, and [yellow] normalized, quenched in oil.

samples. Since the ASS has a crystal structure of face-centered cubic, the planes are focused on (111), (200), (220), and (311). A high peak at the (111) plane is found from the ASS after quench annealing in water and oil. Significant changes are identified in the (311) diffraction plane of ASS after quenching in the air. The (111) peak is prominent for the water- and oil-quenched samples, but the (220) peak is very small in comparison to other peaks. The (311) peak is very strong or prominent for samples cooled in the air as compared to other samples.

Neutron Diffraction HRPD Measurements and Strain Analysis

To confirm the XRD results, the neutron diffraction analysis was conducted, and the results present similar austenite steel synthesized. The neutron diffraction pattern of the base material as shown in Figure 2 below, it is having a cubic Fm3m structure with no extra diffraction peak belonging to the secondary phase and a lattice parameter (a = 0.3592 ± 0.008 nm). The peaks' intensity is sharp and narrow, confirming that the sample is of high quality with good crystallinity and fine grain size. The peaks' indices correspond to the Fm3m space group symmetry, indicating the sample is austenite. In comparison to the XRD pattern in Figure 1a above, the reflection peaks (200) and (220) are very small, also especially in comparison to the (111) and (311) reflection peaks. This result stands in quite a contrast with the XRD pattern of the as-cast sample in Figure 1 above. Therefore, there is a preferred orientation inclination in the sample, as revealed by the HRPD method. Using the obtained HRPD data, the reflection peaks were fitted with the Gaussian function to perform the calculation of the crystallite size and lattice strain parameters.

$$f(x) = ae^{-\frac{(x-b)^2}{2c^2}} \quad (1)$$

The Gaussian fitting function f(x) is the fitting result, a is the fitted maximum intensity of the reflection peak, b is the $2\theta^o$ position of the reflection peak, and c is the FWHM or the β_{hkl}. From Figure 2, it is shown that the Gaussian function fits the diffraction profile very well, and the symmetry of the reflection profile is also very well-defined. The fitting results are shown in Table 2 above.

From the results listed in Table 2, it could be seen that the FWHM values increase with increasing diffraction angles. The Williamson-Hall method was used to determine the crystallite size and the microstrain in a polycrystalline sample to make a comparison with the results obtained from the whole Gaussian fitting. In this case, both the microstrain and the profile broadening due to size can be expressed as the following equation (Mote *et al.* 2012; Dani *et al.* 2017):

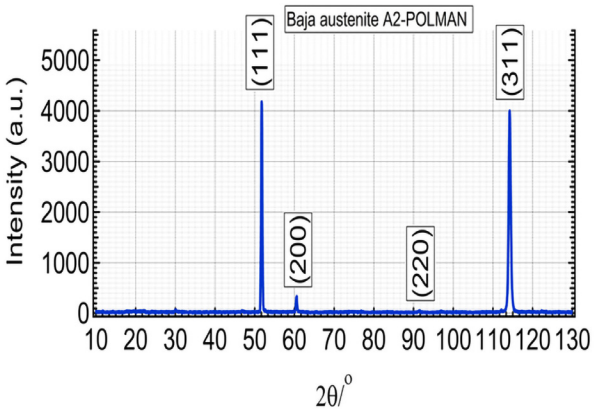

Figure 2. Gaussian Fitting of the reflection intensity profile of the 56Fe25Ni16.6Cr0.9Si0.5Mn ASS as-cast obtained by HRPD Neutron method: [a] (111), [b] (200), and [c] (311) reflection planes.

Table 2. The Gaussian fitting results.

hkl	Å (x10^{-4} nm)	2θ°	$(FWHM)_{hkl}$/°
(111)	3,304.26	51.77	0.19
(200)	265.11	60.53	0.19
(311)	3,728.28	114.23	0.35

$$\beta_{hkl}\cos\theta = \frac{K\lambda}{L} + 4\varepsilon\sin\theta \quad (2)$$

In the above equation, also known alternatively as the UDM, L is the crystallite diameter size (Å), and ε is the average maximum microstrain. Plotting $\beta_{hkl}\cos\theta$, *versus* sin θ, will result in a straight line. The intercept of the regression line with the vertical axis is related to the inverse of the size and the slope is related to the value of the microstrain. From the intercept of linear regression with the vertical axis, crystallite size could be determined and from the slope of the regression line, the microstrain is calculated. The plot is shown in Figure 3 above; K is a constant and equal to 0.9, λ is the neutron wavelength 1.8216 Å, the average grain size D is 65.499 nm, and the deformation strain ε sin θ is 2.3705×10^{-4}.

SEM and EDS Observations of the 56Fe25Ni16.6Cr0.9Si0.5Mn ASS Matrix

Microstructures of the 56Fe25Ni16.6Cr0.9Si0.5Mn ASS as-cast and after treatments are shown in Figure 4. In general, almost all samples consist of grains of γ-austenite, and some particles of carbides either in the interior grains or segregated in the grain boundary. Since the considerable additional elements are C, Ti, and Al contents as the forming of reinforcing particles of γ'-Ni_3(Al, Ti) and the cause of creep, η-Ni_3Ti are very small, the islands and

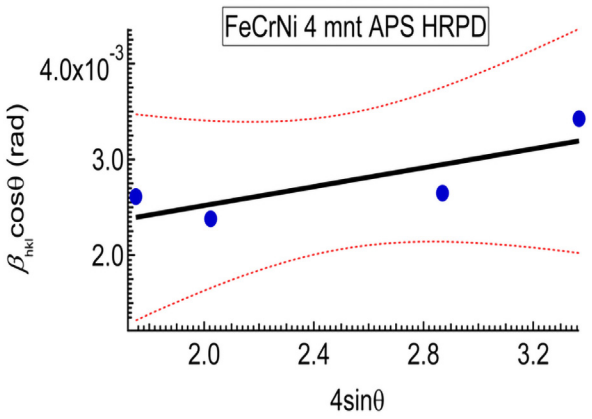

Figure 3. UDM plot of 56Fe25Ni16.6Cr0.9Si0.5Mn ASS.

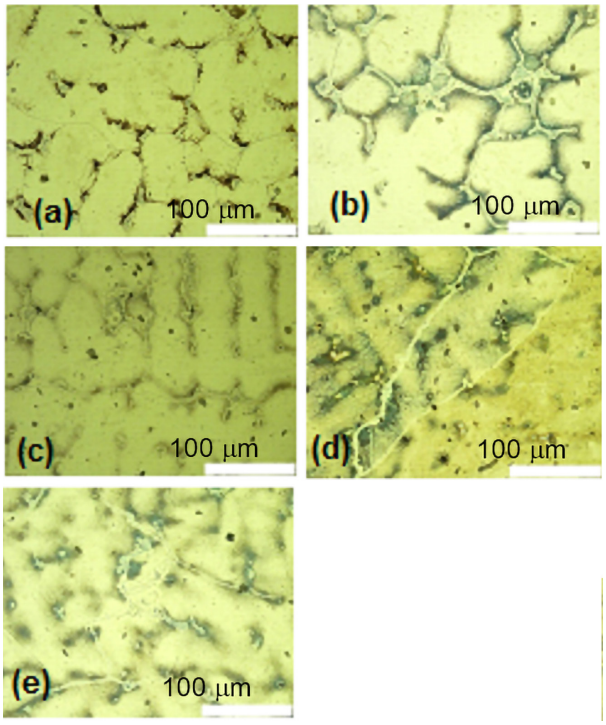

Figure 4. Grain boundaries with 100x magnification optical microscope result in [a] As-cast, annealing, followed by cooling in [b] furnace and [c] air, and quenching in [d] oil and [e] water.

fine particles – which may be formed in the segregation region – are $M_{23}C_6$ and M_7C_3, respectively. The ASS as-cast is composed of γ-austenite grains and some grain boundary islands of $M_{23}C_6$ as identified in its elements in Table 3. The grain boundary expands to be a region with some $M_{23}C_6$ islands in the middle after annealing at a temperature of 1100 °C for a time of 30 min. Some fine particles of M_7C_3 were found in the zone and there are intermetallic particle-free zones near islands and grains. Increasing the cooling rates up to oil quenching decreases the region of the grain boundary. As listed in Table 3, Cr content in the $M_{23}C_6$ islands is higher: in the range of 40–70 %wt. By contrast, Cr content drops to be respectively 16–20 %wt and 15–17 %wt for M_7C_3 precipitates and intermetallic particle-free zones in the grain boundary regions. Moreover, $M_{23}C_6$ formed after normalizing with a high cooling rate in water or oil media becomes more elongated islands.

Table 3. EDS result of all samples on the grain and precipitates.

Sample	Precipitation size	Element (%wt)				
		Fe	Cr	C	Ni	Si
As-cast	Grain	23.0	64.0	8.0	5.0	–
	Precipitates	49.0	18.0	9.0	23.0	1.0
Annealed	Grain	26.0	58.0	8.0	8.0	–
	Precipitates	51.0	20.0	4.0	24.0	1.0
Normalized, cooled in air	Grain	19.0	70.0	9.0	2.0	–
	Precipitates	50.0	19.0	7.0	23.0	1.0
Normalized, quenched in water	Grain	24.0	56.0	14.0	6.0	–
	Precipitates	48.0	16.0	12.0	22.0	2.0
Normalized, quenched in oil	Grain	36.0	40.0	12.0	11.0	–
	Precipitates	49.0	20.0	7.0	22.0	2.0

From all the EDS results, it's shown there's some small element shift that happened in its grains or precipitates. A neat version of these is shown in Table 3. There were also a few elemental shifts that happened on its clean surface without any grain or precipitates. This was called stainless steel base and is shown in Table 4.

As can be seen in Figure 4, the ASS as-cast has a diameter average for grains of about 260.81 µm. Bigger grains of

Table 4. EDS result of all samples on the intermetallic precipitate free zone.

Sample	Element (%wt)				
	Fe	Cr	C	Ni	Si
As-cast	53.0	16.0	3.0	25.0	1.0
Annealed	55.0	16.0	2.0	26.0	1.0
Normalized, cooled in air	53.0	16.0	4.0	25.0	2.0
Normalized, quenched in water	52.0	15.0	8.0	24.0	1.0
Normalized, quenched in oil	54.0	17.0	5.0	24.0	1.0

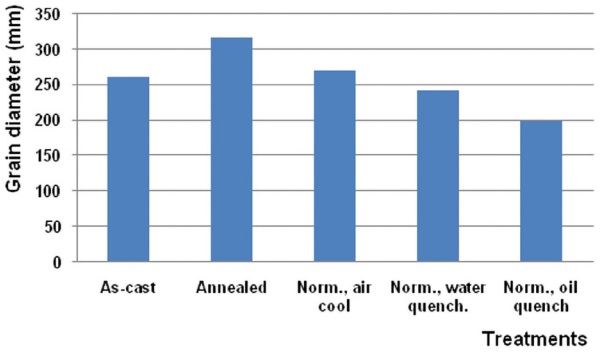

Figure 6. Average grain diameters in the 56Fe25Ni16.6Cr0.9Si0.5Mn ASS as cast and after various treatments.

316 µm were found after annealing at a temperature of 1100 °C for a time of 30 min. However, grain sizes are varied in the ASS after normalizing at the same condition as annealing, followed by cooling in various media such as air, water, or oil. The grain size formed after normalizing and then cooling in the air is about 270.52 µm, whereas normalizing and quenching in water and oil produce grain sizes of about 242.69 and 199.57 µm, respectively. Thus, as compared to the ASS as-cast, the high grain growth in the ASS has occurred in the annealing process. Using air as media after normalizing slightly develops the grains in the ASS. By contrast, the ASS has smaller grains after being normalized and cooled in water or oil.

As can be seen in Figure 5 and based on Table 3, possible islands and particles formed in the grain boundary are $M_{23}C_6$ and M_7C_3, respectively. The diameter average of $M_{23}C_6$ islands in the ASS as-cast is about 2.84 µm. Such islands become bigger to be 4.38 µm during the annealing process. This significant grows also found in the normalizing, which was followed by cooling in air, water, and oil to be 4.20, 3.69, and 4.37 µm, respectively. The particle shape also changes after normalizing to become more elongated as indicated by the roundness factor of above 0.61 to be lower than 0.46. Therefore, besides the modification of particle shapes, all treatments grow $M_{23}C_6$ particles in the grain boundary region of austenite.

As shown in Figures 6 and 7, very fine particles are also found in the grain boundary of austenite. Table 3 confirms that the particles have an M_7C_3 phase, containing about 1–5 %wt Cr and 2–10 %wt C. The precipitate size is lower than 0.26 µm except for the ASS normalized and quenched in oil, which has about 0.36 µm. The shape of the precipitates is close to the equiaxed form and seems relative to be almost similar before and after treatments. This can be seen in the difference between the roundness factor of about 0.05 or the lowest of about 0.60 and the highest of about 0.65.

TEM Measurement Results

The morphologies of the ASS were also observed using the TEM measurements. The TEM bright-field (BF) image is shown in Figure 8, and the alloy with element contents is listed in Table 5.

The TEM results show the steel matrix and the grain boundaries in the austenite steel. The rectangular-shaped and irregularly shaped patches are nano-sized precipitates, which are formed close to the surface area. Therefore, even in the as-cast phase, the precipitates are a prominent feature in the samples. The precipitates form a substantial fraction of the surface area and are mostly oriented. The sizes of the rectangular precipitate ranged from 63 × 32 nm to 84 × 42 nm, with the larger-sized irregulars reaching about 190 nm across. The HRPD Williamson-Hall analysis

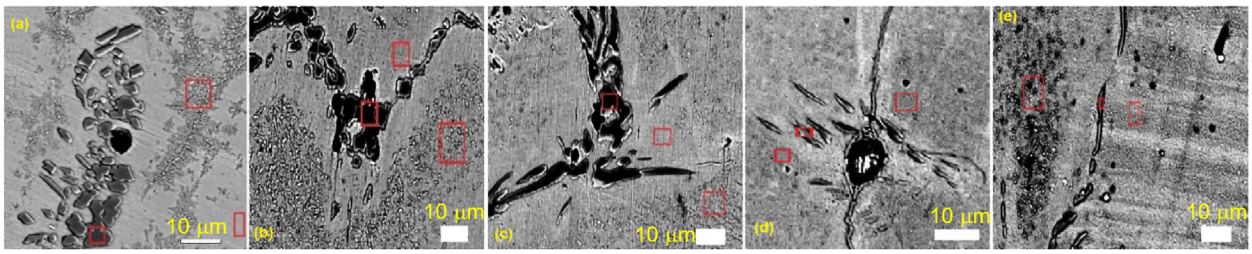

Figure 5. SEM micrographs of [a] As-cast, [b] annealed, [c] normalized, cooled in the air, [d] normalized, quenched in water, and [e] normalized, quenched in oil samples, which show its [1] islands, [2] particles, and [3] intermetallic precipitates free zone.

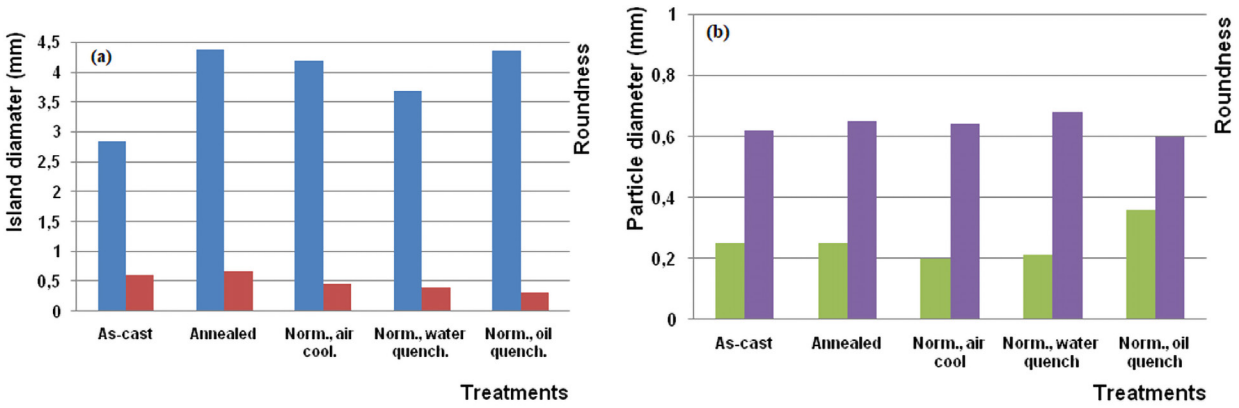

Figure 7. [a] Island and [b] particle diameter and roundness in various treatments.

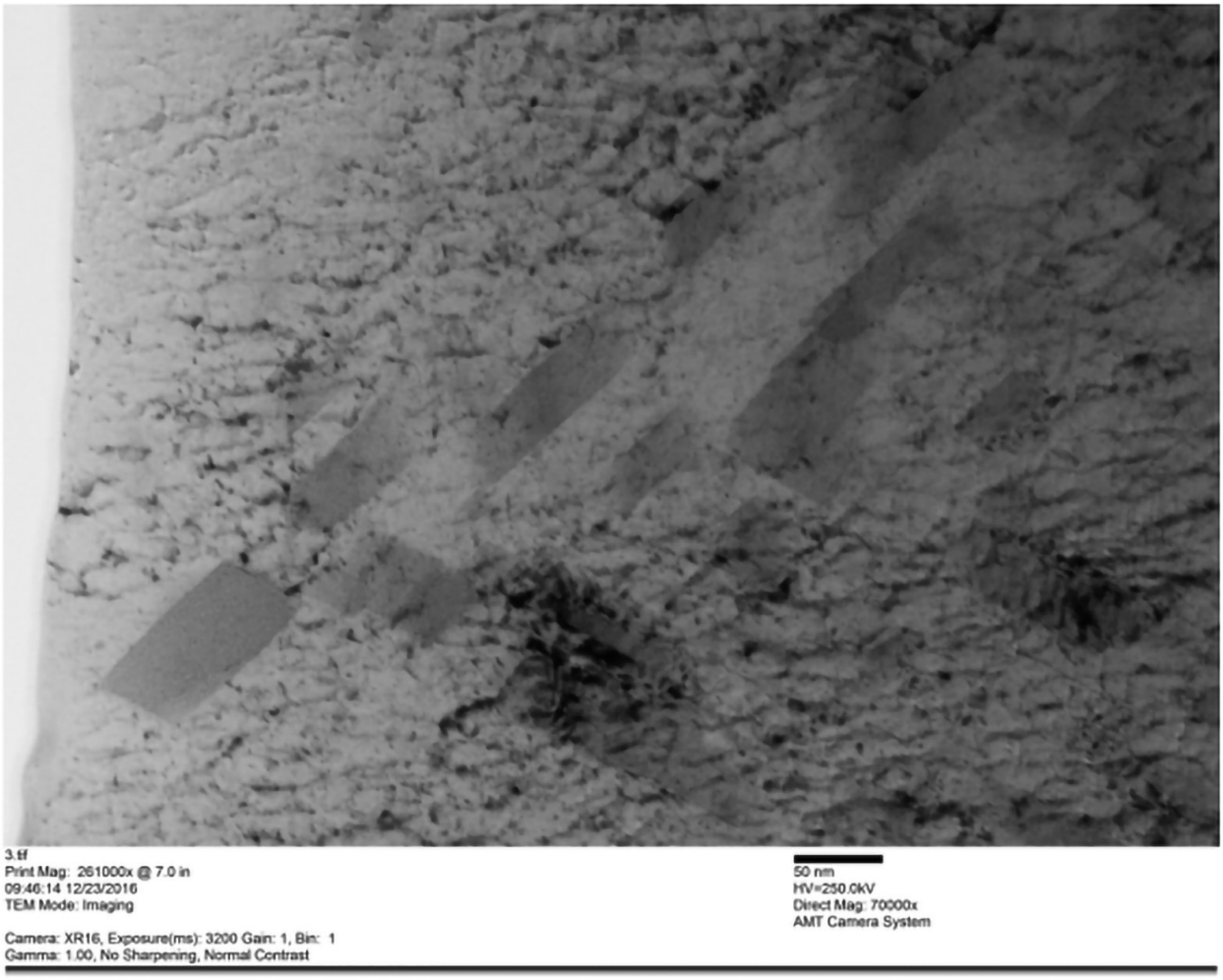

Figure 8. The TEM BF image of 56Fe25Ni16.6Cr0.9Si0.5Mn ASS.

Table 6. FWHM table for planes (111) and (311).

Sample	2θ	FWHM	
		(111)	(311)
As-cast	43.55	0.25	2.02
Annealed	43.71	0.17	1.72
Normalization, cooled in air	43.60	0.75	1.78
Normalization, quenched in water	43.57	0.21	1.72
Normalization, quenched in oil	43.57	0.19	1.37

presented above seems to support this observation. The EDS spectra confirm that in addition to Fe, Cr, and Ni, the W content is also very substantial in the bulk of the samples.

DISCUSSION

The ASS as-cast has been identified to have the main alloying elements Ni and Cr at about 25.04 and 16.55 %wt, respectively. The steel with this composition may be categorized as Fe-Ni-based superalloy (Simsch *et al.* 1987). The minimum Ni content for the superalloy is about 25 %wt and has a function to stabilize γ-austenite in superalloys, which is known to have a positive influence on high temperature (Blaine 2010). A study (Reed and Schramm 1969) about this alloy with close its composition had succeeded to characterize that the γ-austenite structure (γ-Fe, Ni) is face center cubic of the Fm3m type with a lattice parameter of a = 3.581 Å. The XRD results from this study shows in agreement with those of previous studies. The γ-austenite, which is the main phase of the matrix in the ASS also structures face center cubic in the symmetry of cubic space in Fm3m type with a lattice parameter of a = 3.592 Å. The HRPD neutron diffraction results confirm the Fm3m space group symmetry of the 56Fe25Ni16.6Cr0.9Si0.5Mn ASS, as measured by the XRD method, therefore establishing the ASS as austenite. Results of the UDM analysis applied to the HRPD neutron diffraction intensity show that the deformation strain ε sin θ is 2.3705×10^{-4}. Thus, the microstructure of ASS, which is dominated by γ-austenite grains is a characterized structure formed during casting. Moreover, several large islands of high Cr carbide are seen preferentially at the grain boundaries.

A similar structure remains to those of the matrix of the annealed ASS. Annealing causes growth of the grain size of the γ-austenite by 21 %wt, which is bigger than that of the ASS as-cast. Annealing the ASS at a temperature of 1100 °C for 30 min grows the grains of γ-austenite due to this low cooling rate provides more time to develop as compared to other processes. However, the lattice parameter for the γ-austenite was slightly different. These can be seen through the shifting of $2\theta_{111}$ and $2\theta_{311}$, indicating the change of lattice strain orientation. Different media used for cooling produce different lattice parameters of γ-austenite.

The matrix of the ASS after normalizing and followed by cooling in air or quenching in water and oil is still dominated by the grains of γ-austenite. However, high cooling rates like quenching in water or oil form the small size of grains. The γ-austenite grains formed in cooling into water or oil media are much smaller than other cooling. As listed in Table 6, its grain orientation slightly shifts from the peak (111) to (311). The shift of peak (311) shows that the grains of γ-austenite became smaller for the ASS quenched in oil. Moreover, normalizing followed by quenching into water and oil formed more change for the lattice strain in the ASS. Thus, the grain sizes of γ-austenite is strongly dependent on the heat treatment and cooling media performed on the ASS.

Table 5. Composition of 56Fe25Ni16.6Cr0.9Si0.5Mn austenite stainless steel.

Element	Weight %	Atomic %
C	2.09	11.35
O	0.00	0.00
Ne	0.00	0.00
Al	1.70	4.12
Cr	8.55	10.74
Fe	25.16	29.43
Ni	12.99	14.46
Cu	17.02	17.50
W	31.02	11.02
Ga	1.47	1.38

In addition to the cooling process, the final particle morphology, size, and phase evolution can be improved during preparation with process control agents such as stearic acid, the effect of ball weight to powder ratio, and grinding speed (Shashanka and Chaira 2015a).

In addition, the grain boundaries – including the carbide islands and particles at and around the grain boundaries – also change with the applied various cooling media. Structural modifications of grain boundaries are also found in the ASS after the heat treatment with the variation of cooling methods. The grain boundary of the ASS as-cast is meeting part between the γ-austenite grains and some of the islands of $M_{23}C_6$ formed in the grain boundaries since the C content in the ASS is significantly higher

than other the elements of the intermetallic compounds for strengthening particles. After annealing, the $M_{23}C_6$ islands grow larger in the middle, and two different zones were found in the grain boundaries. One zone close to γ-austenite grains and carbide islands of $M_{23}C_6$ is the carbide particles zone, and the other in the middle of the zone is the particle-free zone. The islands tend to grow in a direction so that the shape of $M_{23}C_6$ resembles those of needle-like islands in the ASS that are normalized and quenched in air, water, or oil media. Whereas the particles of M_7C_3 do not seem to grow at all, their shape remains as that of the equiaxed form.

$M_{23}C_6$ islands and the precipitation-free zone around the islands at the grain boundaries of the ASS may be estimated as sources of initiation cracks in the creep process at high temperatures. The risk is also mentioned in a study about the dissolution of grain boundary carbide in cast steel HK30 (Francisco *et al.* 2017). The possibility of crack initiation is smaller for the formation of small islands and thin zone as a result of the Cr deflection at grain boundaries so this formation as formed after normalizing, followed by quenching into water or oil is an ideal structure to inhibit intergranular slip – causing better mechanical properties, especially in strength and creep at the high temperature. The discussion of the $M_{23}C_6$ formation has been also explained in another study of ASS around weld joints by the TIG method (Parikin *et al.* 2017).

The TEM results for the ASS show clearly that even in the as-cast phase, the precipitates are already a prominent feature in the samples. The precipitates form a substantial fraction of the surface area. The sizes of the rectangular precipitate range from 63 × 32 nm to 84 × 42 nm with the larger-sized irregulars reaching about 190 nm across, and the HRPD Williamson-Hall analysis presented above seems to support this observation.

CONCLUSION

The study of the microstructure of ASS developed after annealing and normalizing at 1100 °C for 30 min with different cooling rates yields the following conclusions. The microstructure of the ASS consists of a matrix of γ-austenite and particles of carbides either in the interior grains or grain boundaries. The annealing process increased the grain size of γ-austenite in the ASS compared to the grain size developed during the normalizing process, which was followed by cooling into the air, water, and oil media. $M_{23}C_7$ islands in the grain boundary develop into a larger size after the annealing or normalizing process and are more elongated. There were no significant changes in particle size or shape of M_7C_3 at the ASS grain boundary after annealing or normalizing. The HRPD neutron diffraction results confirmed the Fm3m space group symmetry of the ASS as observed by the XRD method, therefore establishing the ASS as an austenite type SS. Results of the UDM analysis applied to the HRPD neutron diffraction intensity showed that the average grain size D is 65.499 nm, and the deformation strain was 2.3705×10^{-4}. The TEM results for the 56Fe25Ni16.6Cr0.9Si0.5Mn austenite stainless steel showed that the sizes of the rectangular precipitate range from 84 × 42 mm to 63 × 32 nm, with the larger-sized irregulars reaching about 190 nm across and the HRPD Williamson-Hall analysis presented above seems to support this observation.

ACKNOWLEDGMENTS

The authors thank Prof. Dr. Syahbuddin from Universitas Pancasila, Dr. Abu K. Rivai, and Dr. Iwan Sumirat of BRIN, for their advice on this research. They also highly appreciate the kind help and assistance from Dr. Damar and Dr. B. Bundjali from the Faculty of Mathematics and Natural Sciences at Bandung Institute of Technology (ITB). Part of this work was carried out at the Research Center for Nanosciences and Nanotechnology of ITB.

REFERENCES

BHADESHIA HKDH, HONEYCOMBE SR. 2006. Steels: Microstructure and Properties, 3rd Edition. Elsevier Ltd., Oxford, UK.

BLAINE G, HUGO L, XIAO HUANG. 2010. Superalloy: Alloying and Performance. The Materials Information Society, ASM International, Materials Park, Ohio.

CHANDA UK, PADHEE SP, PATHAK AD, ROY S, PATI S. 2019. Effect of Cr content on the corrosion resistance of Ni–Cr–P coatings for PEMFC metallic bipolar plates. Mater Renew Sustain Energy 8(20). https://doi.org/10.1007/s40243-019-0158-8

DANI M, PARIKIN P, DIMYATI A, RIVAI AK, ISKANDAR R. 2018. International Journal of Technology 9(1): 89–98.

DANI M, JAHJAAK, PARIKIN P, INSANI A, ISKANDAR R. 2017. Malaysian Journal of Fundamental and Applied Sciences 13(4): 754–759.

DANI M, UNTORO P, PUTRA TYSP, PARIKIN P, MAYER J, DIMYATI A. 2015. Transmission Electron Microscopy Characterization of High-temperature Oxidation of Fe-20Cr-5Al Alloy Prepared by Focused Ion Beam Technique. Makara Journal of Technology 19(2): 85–89.

DAVID SA, SIEFERT JA, FENG Z. 2013. Welding and weldability of candidate ferritic alloys for future advanced ultrasupercritical fossil power plants. Science and Technology of Welding and Joining 18(8): 631–651.

EFFENDI N, JAHJA AK, BANDRIANA B, ADI WA. 2012. Some Data of Second Sequence Non-standard Austenitic Ingot A2. Urania, Scientific Journal of Nuclear Fuel Cycle 18(1): 48–58

FRANCISCO JGS, JORGE S, RONNY G. 2017. Dissolution of Grain-boundary Carbides by the Effect of Solution Annealing, Heat Treatment, and Aging Treatment on Heat-resistant Cast Steel KH30. Metals 7(7): 251–263.

GUPTA S, SHASHANKA R, CHAIRA D. 2015. Synthesis of nano-structured duplex and ferritic stainless-steel powders by planetary milling: an experimental and simulation study, IOP Conf. Ser.: Mater Sci Eng 75: 012033. DOI 10.1088/1757-899X/75/1/012033

KAZIMIERZ JD. 2015. Analysis of the Precipitation and Growth Processes of the Intermetallic Phases in a Fe-Ni Superalloy.

KADHIM ZD. 2016. Effect of Quenching Media on Mechanical Properties for Medium Carbon Steel. Int Journal of Engineering Research and Application 6(8, Pt 5): 26–34.

MICHAEL M. 2008. Stainless Steels for Design Engineers. ASM International, Materials Park, Ohio, USA.

MOTE VD, PURUSHOTHAM Y, DOLE BN. 2012. Williamson-Hall analysis in estimation of lattice strain in nanometer-sized ZnO particles. Journal of Theoretical and Applied Physics 6: 6.

NAYAK AK, SHASHANKA R, CHAIRA D. 2016. Effect of Nanosize Yttria and Tungsten Addition to Duplex Stainless Steel During High Energy Planetary Milling. IOP Conf Ser: Mater Sci Eng 115: 012008. DOI: 10.1088/1757-899X/115/1/012008

PARIKIN P, DANI M, JAHJA AK, ISKANDAR R, MAYER J. 2018. Crystal Structure Investigation of Ferritic 73Fe24Cr2Si0.8Mn0.1Ni Steel for Multi-purpose Structural Material Applications, International Journal of Technology 9(1): 78–88.

PARIKIN P, ISMOYO AH, DIMYATI A. 2017. Residual Stress Measurements on the TIG-Weldjoint of 57Fe15Cr25Ni Austenitic Steel for Structure Material Applications by Means X-ray Diffraction Techniques. Makara Journal of Technology 21(2): 49–57.

REED RP, SCHRAMM RE. 1969. Lattice Parameter of Martensite and Austenite in Fe-Zn Alloys, Journal of Applied Physics 40(9): 3453–3458.

SHASHANKA R, CHAIRA D. 2014. Phase transformation and microstructure study of nano-structured austenitic and ferritic stainless steel powders prepared by planetary milling. Powder Technology 259: 125–136.

SHASHANKA R, CHAIRA D. 2015a. Development of nano-structured duplex and ferritic stainless steels by pulverisette planetary milling followed by pressureless sintering. Materials Characterization 99: 220–229.

SHASHANKA R, CHAIRA D. 2015b. Optimization of milling parameters for the synthesis of nano-structured duplex and ferritic stainless steel powders by high energy planetary milling. Powder Technology 278: 35–45.

SHASHANKA R, CHAIRA D. 2016. Effects of Nano-Y2O3 and Sintering Parameters on the Fabrication of PM Duplex and Ferritic Stainless Steels. Acta Metall Sin (Engl Lett) 29: 58–71. https://doi.org/10.1007/s40195-015-0362-1

SIMSCH T, STOLOFF NS, HAGEL WS. 1987. Superalloy II. New York: John Wiley & Sons.

WITHERS PJ, BHADESHIA HKDH. 2001. Residual Stress; Part 1 – Measurement techniques. Mat Sci Tech 17(4): 355.

WORLD STEEL ASSOCIATION. 2016 (October). Steel Statistical Yearbook 2016. October 2016. Brussels, Belgium.

XU X, YU Z, HOU C, SONG W, WANG Y. 2017. Microstructure and Properties of Plasma-Nitrided Fe-based Superalloy Fe-25Ni-15Cr. Metallurgy and Materials Transaction A 48A: 3357–3369.